

# SpectroMotion: Dynamic 3D Reconstruction of Specular Scenes

Cheng-De Fan<sup>1</sup> Chen-Wei Chang<sup>1</sup> Yi-Ruei Liu<sup>2</sup> Jie-Ying Lee<sup>1</sup>  
 Jiun-Long Huang<sup>1</sup> Yu-Chee Tseng<sup>1</sup> Yu-Lun Liu<sup>1</sup>

<sup>1</sup>National Yang Ming Chiao Tung University <sup>2</sup>University of Illinois Urbana-Champaign

## Abstract

We present SpectroMotion, a novel approach that combines 3D Gaussian Splatting (3DGS) with physically-based rendering (PBR) and deformation fields to reconstruct dynamic specular scenes. Previous methods extending 3DGS to model dynamic scenes have struggled to represent specular surfaces accurately. Our method addresses this limitation by introducing a residual correction technique for accurate surface normal computation during deformation, complemented by a deformable environment map that adapts to time-varying lighting conditions. We implement a coarse-to-fine training strategy that significantly enhances scene geometry and specular color prediction. It is the only existing 3DGS method capable of synthesizing photorealistic real-world dynamic specular scenes, outperforming state-of-the-art methods in rendering complex, dynamic, and specular scenes. See our project page for video results: <https://cdfan0627.github.io/spectromotion>.

## 1. Introduction

3D Gaussian Splatting (3DGS) [15] has emerged as a ground-breaking technique in 3D scene reconstruction, offering fast training and real-time rendering capabilities. By representing 3D space using a collection of 3D Gaussians and employing a point-based rendering approach, 3DGS has significantly improved efficiency in novel-view synthesis. However, extending 3DGS to model dynamic scenes, especially those containing specular surfaces accurately, has remained a significant challenge.

Existing extensions of 3DGS have made progress in either dynamic scene reconstruction or specular object rendering, but none have successfully combined both aspects. Methods tackling dynamic scenes often struggle with accurately representing specular surfaces, while those focusing on specular rendering are limited to static scenes. This capability gap has hindered the application of 3DGS to real-world scenarios where both motion and specular reflections are present.

We present SpectroMotion, a novel approach that addresses these limitations by combining 3D Gaussian Splatting with physically-based rendering (PBR) and deforma-

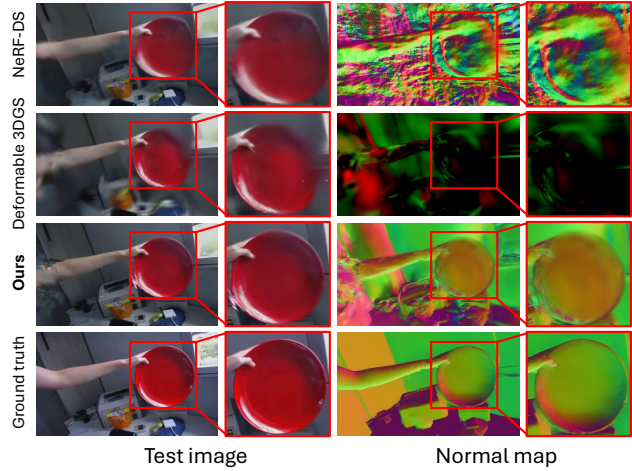


Figure 1. **Our method, SpectroMotion, recovers and renders dynamic scenes with higher-quality reflections compared to prior work.** It introduces physical normal estimation, deformable environment maps, and a coarse-to-fine training strategy to achieve superior results in rendering dynamic scenes with reflections. Here, we present a rendered test image, corresponding normal maps, and a ground-truth image, where the ground-truth normal map (used as a reference) is generated using a pre-trained normal estimator [5]. For Deformable 3DGS, we use the shortest axes of the deformed 3D Gaussians as the normals. We have highlighted the specular regions to demonstrate the effectiveness of our approach.

tion fields. Our method introduces three key innovations: a residual correction technique for accurate surface normal computation during deformation, a deformable environment map that adapts to time-varying lighting conditions, and a coarse-to-fine training strategy that significantly enhances scene geometry and specular color prediction.

Our evaluations demonstrate that SpectroMotion outperforms prior methods in view synthesis of scenes containing dynamic specular objects, as illustrated in Fig. 1. It is the only 3DGS method capable of synthesizing photorealistic real-world dynamic specular scenes, surpassing state-of-the-art techniques in rendering complex, dynamic, and specular content. This advancement represents a significant leap in 3D scene reconstruction, particularly for challenging scenarios involving moving specular objects.

In summary, we make the following contributions:

- We propose SpectroMotion, a physically-based rendering (PBR) approach combining deformation fields and 3D Gaussian Splatting for real-world dynamic specular scenes.
- We introduce a residual correction method for accurate surface normals during deformation, coupled with a deformable environment map to handle time-varying lighting conditions in dynamic scenes.
- We develop a coarse-to-fine training strategy enhancing scene geometry and specular color prediction, outperforming state-of-the-art methods.

## 2. Related Work

### 2.1. Dynamic Scene Reconstruction.

Recent works have leveraged NeRF representations to jointly solve for canonical space and deformation fields in dynamic scenes using RGB supervision [8, 18, 25, 29, 30, 32, 37, 44]. Further advancements in dynamic neural rendering include object segmentation [34], incorporation of depth information [1], utilization of 2D CNNs for scene priors [23, 31], and multi-view video compression [17]. However, these NeRF-based methods are computationally intensive, limiting their practical applications. To address this, 3D Gaussian Splatting [15] has emerged as a promising alternative, offering real-time rendering capabilities while maintaining high visual quality. Building upon this efficient representation, recent research has adapted 3D Gaussians for dynamic scenes [10, 21, 27, 36, 42, 43, 47]. Nevertheless, these approaches do not explicitly account for changes in surface normal during the dynamic process. Our work extends this line of research by combining specular object rendering based on normal estimation with a deformation field, enabling each 3D Gaussian to model dynamic specular scenes effectively.

### 2.2. Reflective Object Rendering.

While significant progress has been made in rendering reflective objects, challenges from complex light interactions persist. Recent years have seen numerous studies addressing these issues, primarily by decomposing appearance into lighting and material properties [2, 3, 16, 28, 35, 39, 52–54]. Building on this foundation, some research has focused on improving the capture and reproduction of specular reflections [26, 38, 40, 49]. In contrast, others have leveraged signed distance functions (SDFs) to enhance normal estimation [7, 19, 20, 24, 51]. The emergence of 3D Gaussian Splatting (3DGS) has sparked a new wave of techniques [6, 11, 22, 33, 48, 55] that integrate Gaussian splatting with physically-based rendering. Nevertheless, accurately modeling dynamic environments and time-varying specular reflections remains a significant challenge. To address this

limitation, our work introduces a novel approach incorporating a deformable environment map and additional explicit Gaussian attributes specifically designed to capture specular color changes over time.

## 3. Method

**Overview of the approach.** The overview of our method is illustrated in Fig. 2. Given an input monocular video sequence of frames and corresponding camera poses, we design a three-stage approach to reconstruct the dynamic specular scene, as detailed in Sec. 3.2. Accurate specular reflection requires precise normal estimation, so Sec. 3.3 elaborates on how we estimate normals in dynamic scenes. Finally, we introduce the losses used throughout the training process in Sec. 3.4.

### 3.1. Preliminary

**3D Gaussian Splatting.** Each 3D Gaussian is defined by a center position  $\mathbf{x} \in \mathbb{R}^3$  and a covariance matrix  $\Sigma$ . 3D Gaussian Splatting [15] optimizes the covariance matrix using scaling factors  $\mathbf{s} \in \mathbb{R}^3$  and rotation unit quaternion  $\mathbf{r} \in \mathbb{R}^4$ . For novel-view rendering, 3D Gaussians are projected onto 2D camera planes using differentiable splatting [50]:

$$\Sigma' = \mathbf{J} \mathbf{W} \Sigma \mathbf{W}^T \mathbf{J}^T. \quad (1)$$

Pixel colors are computed using point-based volumetric rendering:

$$C = \sum_{i \in N} T_i \alpha_i \mathbf{c}_i, \quad \alpha_i = \sigma_i e^{-\frac{1}{2}(\mathbf{x})^T \Sigma'(\mathbf{x})}, \quad (2)$$

where  $T_i = \prod_{j=1}^{i-1} (1 - \alpha_j)$  is the transmittance,  $\sigma_i$  is the opacity, and  $\mathbf{c}_i$  is the color of each 3D Gaussian.

### 3.2. Specular Rendering

Since accurate reflections depend heavily on precise geometry, we implement a three-stage coarse-to-fine training strategy: static, dynamic, and specular stages. This approach ensures both stable scene geometry and accurate specular rendering.

#### 3.2.1. Coarse-to-Fine Training Strategy

**Static stage.** In the static stage, we employ vanilla 3DGS [15] for static scene reconstruction to stabilize the geometry of the static scene. Specifically, we optimize the position  $\mathbf{x}$ , scaling  $\mathbf{s}$ , rotation  $\mathbf{r}$ , opacity  $\alpha$ , and coefficients of spherical harmonics (SH) of the 3D Gaussians by minimizing the photometric loss  $\mathcal{L}_{\text{color}}$  identical to 3DGS [15].

**Dynamic stage.** Following the static stage, we address dynamic objects using Deformable 3DGS [47]. For each 3D Gaussian in canonical 3D Gaussians  $\mathbf{G}$ , we input its

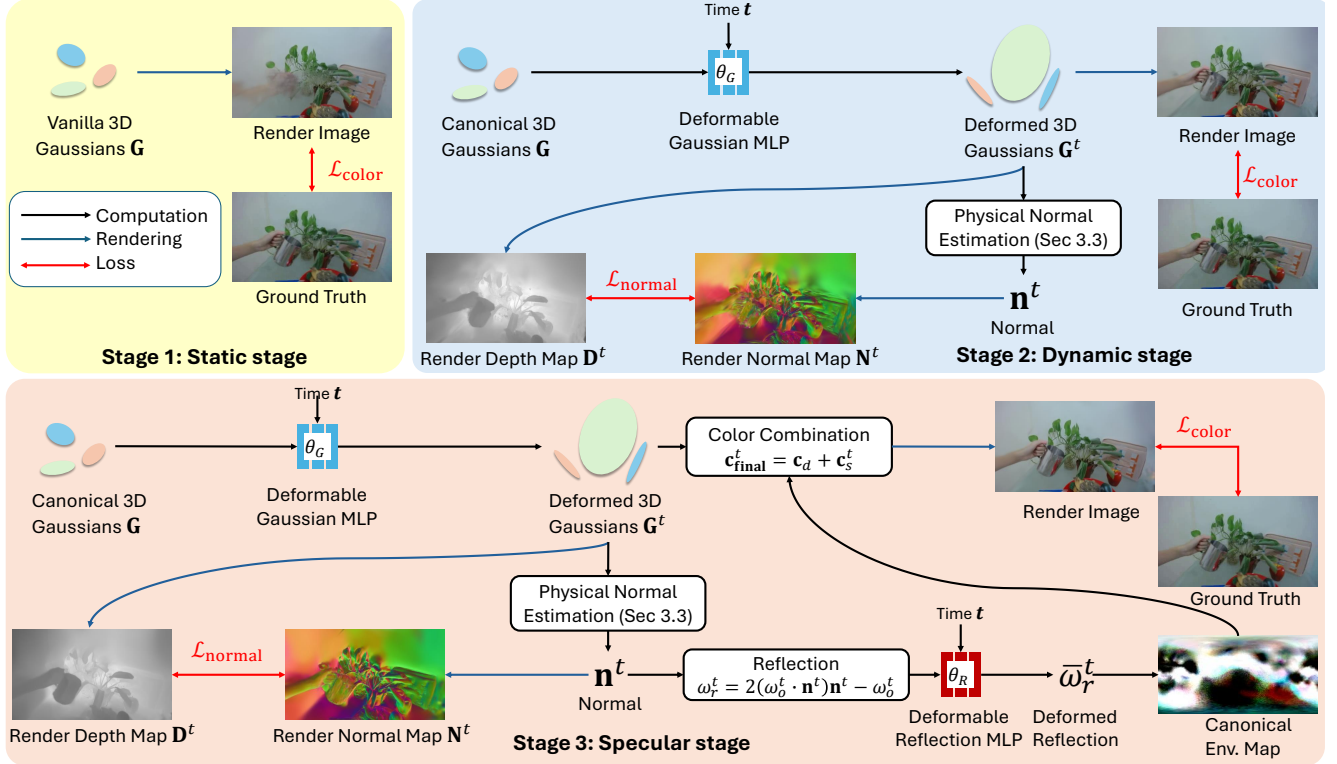


**Figure 2. Method Overview.** Our method stabilizes the scene geometry through three stages. In the static stage, we stabilize the geometry of the static scene by minimizing photometric loss  $\mathcal{L}_{\text{color}}$  between vanilla 3DGS renders and ground truth images. The dynamic stage combines canonical 3D Gaussians  $\mathbf{G}$  with a deformable Gaussian MLP to model dynamic scenes while simultaneously minimizing normal loss  $\mathcal{L}_{\text{normal}}$  between rendered normal map  $\mathbf{N}^t$  and gradient normal map from depth map  $\mathbf{D}^t$ , thus further enhancing the overall scene geometry. Finally, the specular stage introduces a deformable reflection MLP to handle changing environment lighting, deforming reflection directions  $\omega_r^t$  to query a canonical environment map for specular color  $\mathbf{c}_s^t$ . It is then combined with diffuse color  $\mathbf{c}_d$  (using zero-order spherical harmonics) and learnable specular tint  $s_{\text{tint}}$  per 3D Gaussian to obtain the final color  $\mathbf{c}_{\text{final}}^t$ . This approach enables the modeling of dynamic specular scenes and high-quality novel view rendering.

position  $\mathbf{x}$  and time  $t$  into a deformable Gaussian MLP with parameters  $\theta_G$  to predict position, rotation, and scaling residuals:  $(\Delta\mathbf{x}^t, \Delta\mathbf{r}^t, \Delta\mathbf{s}^t) = F_{\theta_G}(\gamma(\mathbf{x}), \gamma(t))$ , where  $\gamma$  denotes positional encoding. Attributes of the corresponding 3D Gaussian in deformed 3D Gaussians  $\mathbf{G}^t$  at time  $t$  is obtained by  $(\mathbf{x}^t, \mathbf{r}^t, \mathbf{s}^t) = (\Delta\mathbf{x}^t, \Delta\mathbf{r}^t, \Delta\mathbf{s}^t) + (\mathbf{x}, \mathbf{r}, \mathbf{s})$ .

This approach separates motion and geometric structural learning, allowing accurate simulation of dynamic behaviors while maintaining a stable geometric reference. To further enhance scene geometry, we estimate normals of deformed 3D Gaussians and optimize them using:

$$\mathcal{L}_{\text{normal}} = 1 - \mathbf{N}^t \cdot \hat{\mathbf{N}}^t, \quad (3)$$

where  $\mathbf{N}^t$  is the rendered normal map and  $\hat{\mathbf{N}}^t$  is the normal map derived from the rendered depth map  $\mathbf{D}^t$ . This process improves local associations among 3D Gaussians and optimizes both depth and normal information across the entire scene.

**Specular stage.** We adopt an image-based lighting (IBL) model with a learnable cube map. Following the rendering equation [13], split-sum approximation [14, 28], and Cook-Torrance reflectance model [4], we formulate the outgoing radiance of the specular component  $L_s$  as:

$$L_s = \int_{\Omega} \frac{DGF}{4(\omega_o^t \cdot \mathbf{n}^t)(\omega_i \cdot \mathbf{n}^t)} (\omega_i \cdot \mathbf{n}^t) d\omega_i \times \int_{\Omega} L_i(\omega_i) D(\omega_i, \omega_o^t) (\omega_i \cdot \mathbf{n}^t) d\omega_i, \quad (4)$$

where  $\Omega$  is the hemisphere around the surface normal  $\mathbf{n}^t$  (describe in Sec. 3.3.)  $D$ ,  $G$ , and  $F$  represent the GGX normal distribution function [41], geometric attenuation, and Fresnel term, respectively.  $\omega_o^t$  is the view direction, and  $L_i(\omega_i)$  is the incident radiance. The first term, we follow GaussianShader [12] directly computed by  $s_{\text{tint}} * F_1 + F_2$ , where  $F_1$  and  $F_2$  are two pre-computed scalars depending on the roughness  $\rho$ , the view direction  $\omega_o^t$  and the normal  $\mathbf{n}^t$ . Roughness  $\rho \in [0, 1]$  and specular tint  $s_{\text{tint}} \in [0, 1]^3$  are learnable parameters for each 3D Gaussian. The second term is pre-integrated in

a filtered learnable cubemap, where each mip-level corresponds to a specific roughness value. After the static and dynamic stages, the geometry is well-defined. This allows us to calculate reflection directions  $\omega_r^t = 2(\omega_o^t \cdot \mathbf{n}^t)\mathbf{n}^t - \omega_o^t$  accurately.

Reflection directions can query the environment map for the specular color of static environment light. To handle time-varying lighting in dynamic scenes, we introduce a deformable environment map, detailed in the following section.

### 3.2.2. Deformable Environment Map for Dynamic Lighting.

The concept of a deformable environment map involves treating the vanilla environment map as a canonical environment map and combining it with a deformation field. This approach enables us to model time-varying lighting conditions effectively. We first apply positional encoding to the reflection direction  $\omega_r^t$  and time  $t$  to implement this. These encoded values are then input into a deformable reflection MLP with parameters  $\theta_R$ . This process allows us to obtain the deformed reflection residual  $\Delta\bar{\omega}_r^t = F_{\theta_R}(\gamma(\omega_r^t), \gamma(t))$  for each specified time  $t$ .

Subsequently, we add the deformed reflection residual  $\Delta\bar{\omega}_r^t$  to the reflection direction  $\omega_r^t$ , yielding the deformed reflection direction  $\bar{\omega}_r^t = \Delta\bar{\omega}_r^t + \omega_r^t$ .

We can then use this deformed reflection direction  $\bar{\omega}_r^t$  to query the canonical environment map, allowing us to obtain time-varying specular color  $\mathbf{c}_s^t$ . This approach effectively captures the dynamic nature of lighting in the scene while maintaining a stable canonical reference.

### 3.2.3. Color Decomposition and Staged Training Strategy.

We decompose the final color  $\mathbf{c}_{\text{final}}^t$  into diffuse and specular components to better distinguish between high and low-frequency information:  $\mathbf{c}_{\text{final}}^t = \mathbf{c}_d + \mathbf{c}_s^t$ , where  $\mathbf{c}_d$  is the diffuse color (using zero-order spherical harmonics as view-independent color), and  $\mathbf{c}_s^t$  is the view-dependent color component. To manage the transition from spherical harmonics to  $\mathbf{c}_{\text{final}}^t$  and mitigate potential geometry disruptions, in the early specular stage, we fix the deformable Gaussian MLP and most 3D Gaussian attributes, optimizing only zero-order SH, specular tint, and roughness. We temporarily suspend densification during this phase. As  $\mathbf{c}_{\text{final}}^t$  becomes more complete, we gradually resume optimization of all parameters and reinstate the densification process.

We further split the specular stage into two parts, applying a coarse-to-fine strategy to the environment map. In the first part, we focus on optimizing the canonical environment map for time-invariant lighting. This establishes a stable foundation for the overall lighting structure. In the second part, we proceed to optimize the deformable reflection MLP for dynamic elements. This approach ensures a more robust learning process, allowing us to capture the static lighting

conditions before introducing the complexities of dynamic components.

## 3.3. Physical Normal Estimation

**Challenges in normal estimation for 3D Gaussians.** Normal estimation is essential for modeling specular objects in 3D Gaussians, where GaussianShader [11] initially used the shortest axis combined with a residual normal for approximation. While this works for static scenes, it becomes problematic with deformed Gaussians because the residual should vary at each time step. A straightforward approach of rotating the residual normal based on quaternion differences between canonical and deformed states proves insufficient, as it doesn't account for shape changes during deformation. When deformation alters the relative axis lengths, the shortest axis assumption breaks down. This highlights the need for a more comprehensive approach that considers both rotational and shape deformation effects to achieve accurate normal estimation for dynamic specular objects.

**Improved rotation calculation for deformed 3D Gaussians.** To overcome the limitations of naive methods and accurately model the normal of deformed 3D Gaussians, we propose using both the shortest and longest axes of canonical and deformed Gaussians to compute the rotation matrix. This approach accounts for both rotation and shape changes during deformation. We first align the deformed Gaussian's axes with those of the canonical Gaussian using the following method:

$$\mathbf{v}_s^t = \begin{cases} \mathbf{v}_s^t & \text{if } \mathbf{v}_s \cdot \mathbf{v}_s^t > 0, \\ -\mathbf{v}_s^t & \text{otherwise.} \end{cases}, \quad \mathbf{v}_l^t = \begin{cases} \mathbf{v}_l^t & \text{if } \mathbf{v}_l \cdot \mathbf{v}_l^t > 0, \\ -\mathbf{v}_l^t & \text{otherwise.} \end{cases}, \quad (5)$$

where  $\mathbf{v}_s$  and  $\mathbf{v}_l$  represent the shortest and longest axes of canonical 3D Gaussians, while  $\mathbf{v}_s^t$  and  $\mathbf{v}_l^t$  denote the same for deformed 3D Gaussians. We then construct orthogonal matrices using these aligned axes and their cross-products:

$$\mathbf{U} = [\mathbf{v}_s \quad \mathbf{v}_l \quad \mathbf{v}_s \times \mathbf{v}_l], \quad \mathbf{V}^t = [\mathbf{v}_s^t \quad \mathbf{v}_l^t \quad \mathbf{v}_s^t \times \mathbf{v}_l^t]. \quad (6)$$

Finally, we derive the rotation matrix  $\mathbf{R}^t = \mathbf{V}^t \mathbf{U}^\top$ .

**Adjusting normal residuals and ensuring accuracy.** To account for shape changes during deformation, we scale the normal residual based on the ratio of oblateness  $\frac{\beta}{\beta^t}$  between canonical and deformed 3D Gaussians.

$$\beta = \frac{|\mathbf{v}_l| - |\mathbf{v}_s|}{|\mathbf{v}_l|}, \quad \beta^t = \frac{|\mathbf{v}_l^t| - |\mathbf{v}_s^t|}{|\mathbf{v}_l^t|}, \quad (7)$$

where  $\beta$  and  $\beta^t$  represent the oblateness of canonical and deformed 3D Gaussians, respectively. This is because flatter 3D

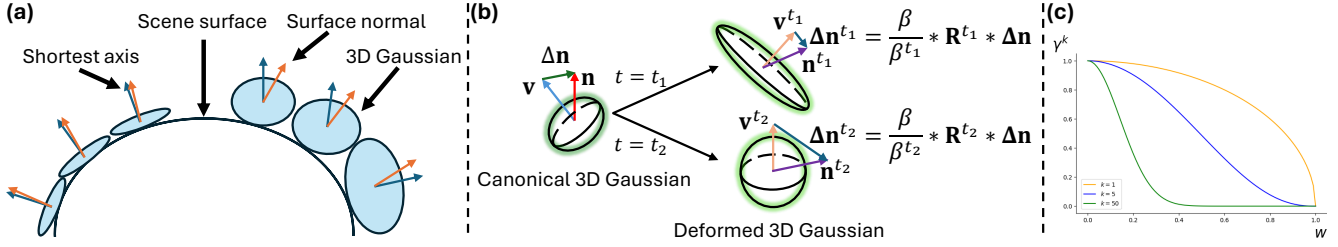


Figure 3. **Normal estimation.** (a) shows that flatter 3D Gaussians align better with scene surfaces, their shortest axis closely matching the surface normal. In contrast, less flat 3D Gaussians fit less accurately, with their shortest axis diverging from the surface normal. (b) shows that when the deformed 3D Gaussian becomes flatter ( $t = t_1$ ), normal residual  $\Delta n$  is rotated by  $R_1^t$  and scaled down by  $\frac{\beta}{\beta t_1}$ , as flatter Gaussians require smaller normal residuals. Conversely, when the deformation results in a less flat shape ( $t = t_2$ ),  $\Delta n$  is rotated by  $R_2^t$  and amplified by  $\frac{\beta}{\beta t_2}$ , requiring a larger correction to align the shortest axis with the surface normal. (c) shows how  $\gamma^k$  changes with  $w$  (where  $w = \frac{|\mathbf{v}_i^t|}{|\mathbf{v}_i^s|}$ ) for  $k = 1$ ,  $k = 5$ , and  $k = 50$ . Larger  $w$  indicates less flat Gaussians, while smaller  $w$  represents flatter Gaussians. As  $k$  increases,  $\gamma^k$  decreases more steeply as  $w$  rises. For  $k = 5$ , we observe a balanced behavior:  $\gamma^k$  approaches 1 for low  $w$  and 0 for high  $w$ , providing a nuanced penalty adjustment across different Gaussian shapes.

Gaussians tend to align more closely with the surface, meaning their shortest axis becomes more aligned with the surface normal, as shown in Fig. 3 (a). In such cases, less compensation from the normal residual is needed. Conversely, less flat Gaussians require more compensation, as illustrated in Fig. 3 (b). We then obtain deformed normal residuals:

$$\Delta \mathbf{n}^t = \frac{\beta}{\beta^t} \mathbf{R}^t \Delta \mathbf{n}. \quad (8)$$

The final normal  $\mathbf{n}^t$  is computed by adding this residual to the shortest axis and ensuring outward orientation:

$$\mathbf{n}^t = \Delta \mathbf{n}^t + \mathbf{v}_s^t, \quad \mathbf{n}^t = \begin{cases} \mathbf{n}^t & \text{if } \mathbf{n}^t \cdot \omega_o^t > 0, \\ -\mathbf{n}^t & \text{otherwise.} \end{cases} \quad (9)$$

This approach adjusts for Gaussian flatness and ensures accurate normal estimation.

### 3.4. Loss Functions

**Normal regularization.** To allow the normal residual to correct the normal while not excessively influencing the optimization of the shortest axis towards the surface normal, we introduce a penalty term for the normal residual:

$$\mathcal{L}_{\text{reg}} = \gamma^k \|\Delta \mathbf{n}\|_2^2 \quad \text{where} \quad \gamma = \sqrt{1 - \frac{|\mathbf{v}_s^t|^2}{|\mathbf{v}_i^t|^2}}. \quad (10)$$

In our experiments, we set  $k = 5$ . When  $k = 5$ , less flat 3D Gaussians have  $\gamma^k$  approaching 0. Their shortest axis aligns poorly with the surface normal, requiring more normal residual correction and smaller penalties. Conversely, flatter Gaussians have  $\gamma^k$  near 1. Their shortest axis aligns better with the surface normal, needing less normal residual correction and allowing larger penalties, as shown in Fig. 3 (c).

**Total training loss.** To refine all parameters in the dynamic and specular stages, we employ the total training loss:

$$\mathcal{L} = \mathcal{L}_{\text{color}} + \lambda_{\text{normal}} \mathcal{L}_{\text{normal}} + \mathcal{L}_{\text{reg}}, \quad (11)$$

where  $\mathcal{L}_{\text{color}}$  and  $\mathcal{L}_{\text{normal}}$  are obtained as described in Section 3.2.1. In our experiments, we set  $\lambda_{\text{normal}} = 0.01$ . Due to space constraints, complete implementation details are provided in the supplementary materials.

## 4. Experiments

### 4.1. Evaluation Results

We evaluate our method on two real-world datasets: NeRF-DS dataset [45] and HyperNeRF dataset [30]. While GaussianShader [11] and GS-IR [22] are originally designed for static scenes and are included here only as reference baselines, we train our method and all baseline approaches for 40,000 iterations to ensure fair comparison.

**NeRF-DS dataset.** The NeRF-DS dataset [45] is a monocular video dataset comprising seven real-world scenes from daily life featuring various types of moving or deforming specular objects. We compare our method with the most relevant state-of-the-art approaches. As shown in Tab. 1 and Fig. 4, the quantitative results demonstrate that our method decisively outperforms baselines in reconstructing and rendering real-world highly reflective dynamic scenes.

The rendering speed is correlated with the quantity of 3D Gaussians. When the number of 3D Gaussians is below 178k, our method can achieve real-time rendering over 30 FPS on an NVIDIA RTX 4090.

**HyperNeRF dataset.** The HyperNeRF dataset contains real-world dynamic scenes and does not include specular objects. As shown in Tab. 2 and Fig. 5, the results demonstrate that we are on par with state-of-the-art techniques for

Table 1. **Quantitative comparison on the NeRF-DS [45] dataset.** We report the average PSNR, SSIM, and LPIPS (VGG) of several previous models on test images. The **best**, the **second best**, and **third best** results are denoted by red, orange, yellow.

Method	As			Basin			Bell			Cup		
	PSNR↑	SSIM↑	LPIPS↓									
Deformable 3DGS [47]	26.04	0.8805	0.1850	19.53	0.7855	0.1924	23.96	0.7945	0.2767	24.49	0.8822	0.1658
4DGS [43]	24.85	0.8632	0.2038	19.26	0.7670	0.2196	22.86	0.8015	0.2061	23.82	0.8695	0.1792
GaussianShader [11]	21.89	0.7739	0.3620	17.79	0.6670	0.4187	20.69	0.8169	0.3024	20.40	0.7437	0.3385
GS-IR [22]	21.58	0.8033	0.3033	18.06	0.7248	0.3135	20.66	0.7829	0.2603	20.34	0.8193	0.2719
NeRF-DS [45]	25.34	0.8803	0.2150	20.23	0.8053	0.2508	22.57	0.7811	0.2921	24.51	0.8802	0.1707
HyperNeRF [30]	17.59	0.8518	0.2390	22.58	0.8156	0.2497	19.80	0.7650	0.2999	15.45	0.8295	0.2302
Ours	26.80	0.8851	0.1761	19.75	0.7922	0.1896	25.46	0.8497	0.1600	24.65	0.8879	0.1588

Method	Plate			Press			Sieve			Mean		
	PSNR↑	SSIM↑	LPIPS↓									
Deformable 3DGS [47]	19.07	0.7352	0.3599	25.52	0.8594	0.1964	25.37	0.8616	0.1643	23.43	0.8284	0.2201
4DGS [43]	18.77	0.7709	0.2721	24.82	0.8355	0.2255	25.16	0.8566	0.1745	22.79	0.8235	0.2115
GaussianShader [11]	14.55	0.6423	0.4955	19.97	0.7244	0.4507	22.58	0.7862	0.3057	19.70	0.7363	0.3819
GS-IR [22]	15.98	0.6969	0.4200	22.28	0.8088	0.3067	22.84	0.8212	0.2236	20.25	0.7796	0.2999
NeRF-DS [45]	19.70	0.7813	0.2974	25.35	0.8703	0.2552	24.99	0.8705	0.2001	23.24	0.8384	0.2402
HyperNeRF [30]	21.22	0.7829	0.3166	16.54	0.8200	0.2810	19.92	0.8521	0.2142	19.01	0.8167	0.2615
Ours	20.84	0.8180	0.2198	26.49	0.8665	0.1889	25.22	0.8712	0.1513	24.17	0.8529	0.1778

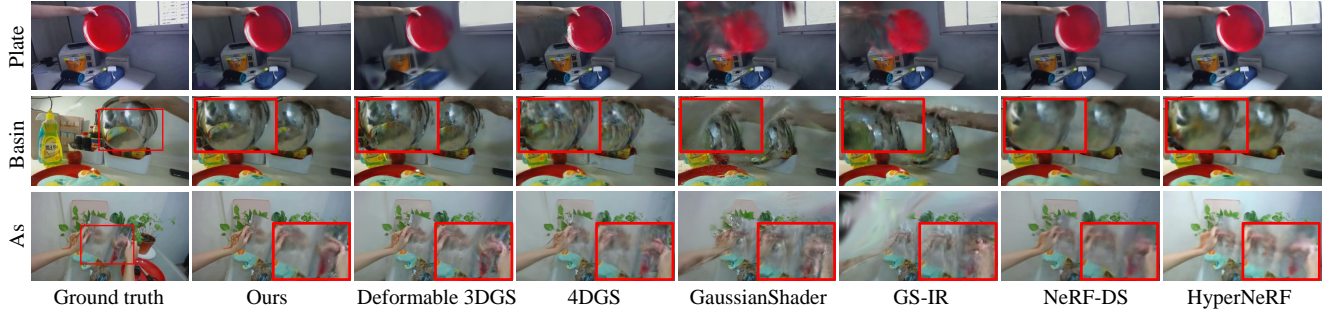


Figure 4. Qualitative comparison on the NeRF-DS [45] dataset.

Table 2. **Quantitative comparison on the HyperNeRF [30] dataset.** We report the average PSNR, SSIM, and LPIPS (VGG) of several previous models. The **best**, the **second best**, and **third best** results are denoted by red, orange, yellow.

Method	PSNR ↑	SSIM ↑	LPIPS ↓
Deformable 3DGS [47]	22.78	0.6201	0.3380
4DGS [43]	24.89	0.6781	0.3422
GaussianShader [11]	18.55	0.5452	0.4795
GS-IR [22]	19.87	0.5729	0.4498
NeRF-DS [45]	23.65	0.6405	0.3972
HyperNeRF [30]	23.11	0.6387	0.3968
Ours	22.18	0.6016	0.3143

rendering novel views, and our method’s performance is not limited to shiny scenes.

In Fig. 6, we compare our method’s normal maps with

those from Deformable 3DGS [47] and NeRF-DS [45]. For Deformable 3DGS [47], we obtain the normals by using the shortest axes of the deformed 3D Gaussians. As demonstrated, our method produces significantly better quality normal maps compared to Deformable 3DGS [47] and NeRF-DS [45].

## 4.2. Ablation Study

For a fair comparison, we train our method and all ablation experiments for 40,000 iterations.

**Different coarse to fine training strategy stages.** As shown in Tab. 3 and Fig. 7, each stage contributes effectively to the model’s performance. The Dynamic stage enhances dynamic object stability compared to the Static stage alone, while the Specular stage improves reflection clarity beyond the combined Static and Dynamic stages.



Figure 5. Qualitative comparison on the HyperNeRF [30] dataset.

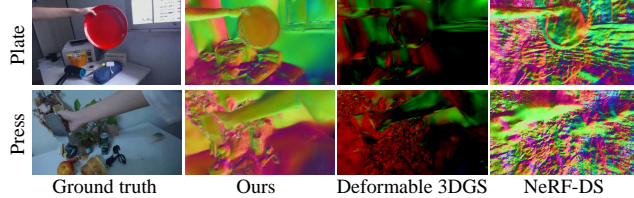


Figure 6. Qualitative comparison of normal maps between our method, Deformable 3DGS, and NeRF-DS.

Table 3. Ablation studies on different coarse to fine training strategy stages.

Stage	PSNR $\uparrow$	SSIM $\uparrow$	LPIPS $\downarrow$
Static	20.26	0.7785	0.2953
St. + Dynamic	24.02	0.8508	0.1831
St. + Dy. + Specular	<b>24.17</b>	<b>0.8529</b>	<b>0.1778</b>

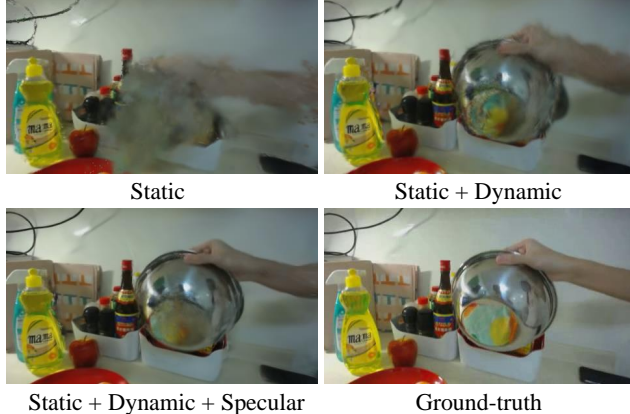


Figure 7. Qualitative comparison of each training stage in our coarse-to-fine approach.

**Ablation study on coarse-to-fine, and loss function.** The model’s performance was evaluated without key components: the coarse-to-fine training strategy, normal loss  $\mathcal{L}_{\text{normal}}$ , normal regularization  $\mathcal{L}_{\text{reg}}$ , and  $\gamma^k$ . Fig. 8 and Tab. 4 illustrate the effects of these omissions. Without the coarse-to-fine approach, the model, trained directly at the specular stage,

Table 4. Ablation studies on different coarse to fine training strategy stages.

C2F	$\mathcal{L}_{\text{normal}}$	$\mathcal{L}_{\text{reg}}$	$\gamma^k$	PSNR $\uparrow$	SSIM $\uparrow$	LPIPS $\downarrow$
	✓	✓	✓	23.16	0.8294	0.2156
✓				23.40	0.8277	0.2278
✓	✓			24.15	0.8510	0.1845
✓	✓	✓		24.09	0.8515	0.1818
✓	✓	✓	✓	<b>24.17</b>	<b>0.8529</b>	<b>0.1778</b>

Table 5. Ablation studies on SH, Static and Deformable environment map.

	PSNR $\uparrow$	SSIM $\uparrow$	LPIPS $\downarrow$
SH	23.63	0.8453	0.1844
Static Env. map	24.02	0.8508	0.1831
Deformable Env. map	<b>24.17</b>	<b>0.8529</b>	<b>0.1778</b>

produces incomplete scene geometry, affecting environment map queries for specular color. Omitting normal loss  $\mathcal{L}_{\text{normal}}$  removes direct supervision on normals and leads to inaccurate reflection directions and less precise specular colors. Removing normal regularization  $\mathcal{L}_{\text{reg}}$  allows the normal residual to dominate normal optimization, resulting in insufficient optimization of the 3D Gaussians’ shortest axis towards the correct normal, which in turn reduces the rendering quality. The normal residual decreases for non-flattened and flat Gaussians without  $\gamma^k$  in normal regularization. This particularly affects less flat 3D Gaussians whose shortest axis significantly deviates from the surface normal. The insufficient normal residual correction causes these 3D Gaussians’ shortest axes to deviate greatly from their original direction in an attempt to align with the surface normal, ultimately reducing rendering quality.

**Ablation study on SH, Static environment map, and Deformable environment map.** Fig. 9 and Tab. 5 demonstrate the superiority of the deformable environment map over the static environment map, which in turn outperforms Spherical Harmonics (SH). SH struggles to accurately model

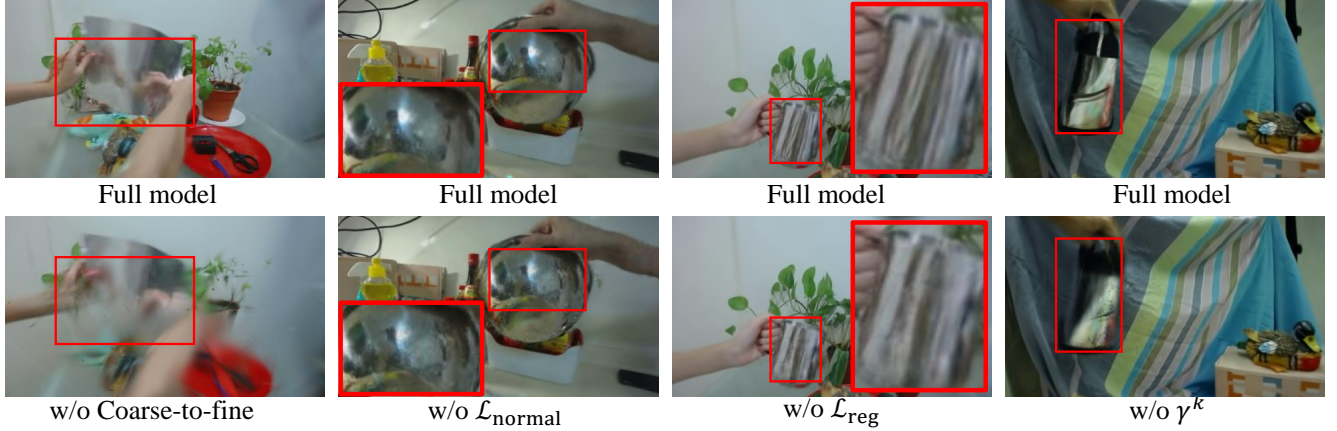


Figure 8. Qualitative comparison of ablation study without different components.

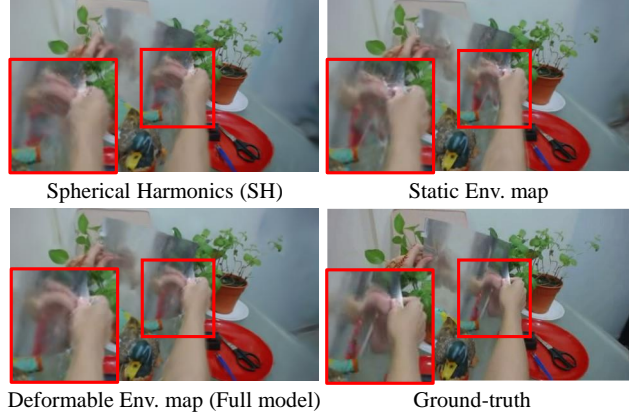


Figure 9. Qualitative comparison of ablation study on SH, Static environment map, and Deformable environment map.

Table 6. Ablation studies on 2DGS and without Physical Normal Estimation.

	PSNR $\uparrow$	SSIM $\uparrow$	LPIPS $\downarrow$
2DGS [9]	23.22	0.8219	0.2283
w/o N.E.	23.89	0.8490	0.1837
Full model	<b>24.17</b>	<b>0.8529</b>	<b>0.1778</b>

high-frequency specular colors. While the static environment map can model high-frequency colors, it is best suited for static lighting conditions. In contrast, the deformable environment map models time-varying lighting, offering superior performance for dynamic scenes.

**Ablation study on 2DGS [9] and without Physical Normal Estimation.** In Fig. 10 and Tab. 6, "2DGS" represents replacing our 3D Gaussian with 2D Gaussian representation. Since 2DGS inherently includes normals, we omit physical normal estimation. "w/o N.E." means skipping physical nor-

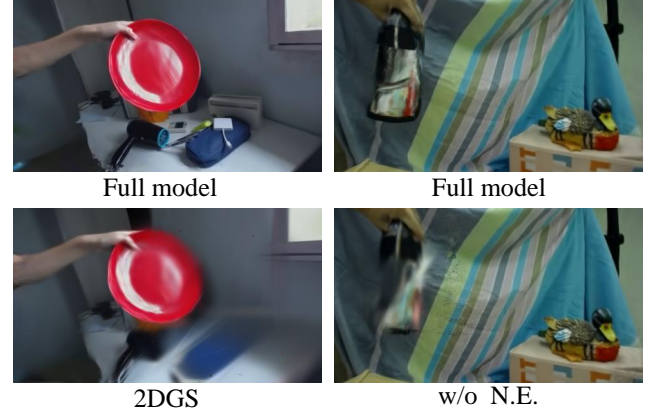


Figure 10. Qualitative comparison of ablation study on 2DGS and without Physical Normal Estimation.

mal estimation and using the shortest axis of 3D Gaussians as the normal. This causes the normal loss  $\mathcal{L}_{\text{normal}}$  to directly supervise the shortest axes, making some axes deviate significantly to align with surface normals, resulting in degraded rendering quality.

## 5. Conclusion

SpectroMotion enhances 3D Gaussian Splatting for dynamic specular scenes by combining specular rendering with deformation fields. Using normal residual correction, coarse-to-fine training, and deformable environment map, it achieves superior accuracy and visual quality in novel view synthesis, outperforming existing methods while maintaining geometric consistency.

**Limitations.** Though we stabilize the entire scene's geometry using a coarse-to-fine training strategy, some failure cases still occur. Please refer to the supplementary materials for visual results of failure cases.

## References

- [1] Benjamin Attal, Eliot Laidlaw, Aaron Gokaslan, Changil Kim, Christian Richardt, James Tompkin, and Matthew O’Toole. Törf: Time-of-flight radiance fields for dynamic scene view synthesis, 2021. 2
- [2] Sai Bi, Zexiang Xu, Pratul Srinivasan, Ben Mildenhall, Kalyan Sunkavalli, Miloš Hašan, Yannick Hold-Geoffroy, David Kriegman, and Ravi Ramamoorthi. Neural reflectance fields for appearance acquisition, 2020. 2
- [3] Mark Boss, Varun Jampani, Raphael Braun, Ce Liu, Jonathan T. Barron, and Hendrik P. A. Lensch. Neural-pil: Neural pre-integrated lighting for reflectance decomposition, 2021. 2
- [4] Robert L Cook and Kenneth E. Torrance. A reflectance model for computer graphics. *ACM Transactions on Graphics (ToG)*, 1(1):7–24, 1982. 3
- [5] Ainaz Eftekhari, Alexander Sax, Jitendra Malik, and Amir Zamir. Omnidata: A scalable pipeline for making multi-task mid-level vision datasets from 3d scans. In *Proceedings of the IEEE/CVF International Conference on Computer Vision*, pages 10786–10796, 2021. 1
- [6] Jian Gao, Chun Gu, Youtian Lin, Hao Zhu, Xun Cao, Li Zhang, and Yao Yao. Relightable 3d gaussian: Real-time point cloud relighting with brdf decomposition and ray tracing. *arXiv preprint arXiv:2311.16043*, 2023. 2
- [7] Wenhong Ge, Tao Hu, Haoyu Zhao, Shu Liu, and Ying-Cong Chen. Ref-neus: Ambiguity-reduced neural implicit surface learning for multi-view reconstruction with reflection, 2023. 2
- [8] Xiang Guo, Jiadai Sun, Yuchao Dai, Guanying Chen, Xiaqing Ye, Xiao Tan, Errui Ding, Yumeng Zhang, and Jingdong Wang. Forward flow for novel view synthesis of dynamic scenes, 2023. 2
- [9] Binbin Huang, Zehao Yu, Anpei Chen, Andreas Geiger, and Shenghua Gao. 2d gaussian splatting for geometrically accurate radiance fields. In *ACM SIGGRAPH 2024 Conference Papers*, pages 1–11, 2024. 8
- [10] Yi-Hua Huang, Yang-Tian Sun, Ziyi Yang, Xiaoyang Lyu, Yan-Pei Cao, and Xiaojuan Qi. Sc-gs: Sparse-controlled gaussian splatting for editable dynamic scenes, 2024. 2
- [11] Yingwenqi Jiang, Jiadong Tu, Yuan Liu, Xifeng Gao, Xiaoxiao Long, Wenping Wang, and Yuexin Ma. Gaussianshader: 3d gaussian splatting with shading functions for reflective surfaces. *arXiv preprint arXiv:2311.17977*, 2023. 2, 4, 5, 6, 12, 14
- [12] Yingwenqi Jiang, Jiadong Tu, Yuan Liu, Xifeng Gao, Xiaoxiao Long, Wenping Wang, and Yuexin Ma. Gaussianshader: 3d gaussian splatting with shading functions for reflective surfaces. In *Proceedings of the IEEE/CVF Conference on Computer Vision and Pattern Recognition*, pages 5322–5332, 2024. 3
- [13] James T Kajiya. The rendering equation. In *Proceedings of the 13th annual conference on Computer graphics and interactive techniques*, pages 143–150, 1986. 3
- [14] Brian Karis and Epic Games. Real shading in unreal engine 4. *Proc. Physically Based Shading Theory Practice*, 4(3):1, 2013. 3
- [15] Bernhard Kerbl, Georgios Kopanas, Thomas Leimkühler, and George Drettakis. 3d gaussian splatting for real-time radiance field rendering, 2023. 1, 2, 11
- [16] Junxuan Li and Hongdong Li. Neural reflectance for shape recovery with shadow handling, 2022. 2
- [17] Tianye Li, Mira Slavcheva, Michael Zollhoefer, Simon Green, Christoph Lassner, Changil Kim, Tanner Schmidt, Steven Lovegrove, Michael Goesele, Richard Newcombe, and Zhaoyang Lv. Neural 3d video synthesis from multi-view video, 2022. 2
- [18] Zhengqi Li, Simon Niklaus, Noah Snavely, and Oliver Wang. Neural scene flow fields for space-time view synthesis of dynamic scenes, 2021. 2
- [19] Ruofan Liang, Huiting Chen, Chunlin Li, Fan Chen, Selvakumar Panneer, and Nandita Vijaykumar. Envidr: Implicit differentiable renderer with neural environment lighting, 2023. 2
- [20] Ruofan Liang, Jiahao Zhang, Haoda Li, Chen Yang, Yushi Guan, and Nandita Vijaykumar. Spidr: Sdf-based neural point fields for illumination and deformation, 2023. 2
- [21] Yiqing Liang, Numair Khan, Zhengqin Li, Thu Nguyen-Phuoc, Douglas Lanman, James Tompkin, and Lei Xiao. Gaufre: Gaussian deformation fields for real-time dynamic novel view synthesis, 2023. 2
- [22] Zhihao Liang, Qi Zhang, Ying Feng, Ying Shan, and Kui Jia. Gs-ir: 3d gaussian splatting for inverse rendering. *arXiv preprint arXiv:2311.16473*, 2023. 2, 5, 6, 12, 14
- [23] Haotong Lin, Sida Peng, Zhen Xu, Yunzhi Yan, Qing Shuai, Hujun Bao, and Xiaowei Zhou. Efficient neural radiance fields for interactive free-viewpoint video, 2022. 2
- [24] Yuan Liu, Peng Wang, Cheng Lin, Xiaoxiao Long, Jiepeng Wang, Lingjie Liu, Taku Komura, and Wenping Wang. Nero: Neural geometry and brdf reconstruction of reflective objects from multiview images, 2023. 2
- [25] Yu-Lun Liu, Chen Gao, Andreas Meuleman, Hung-Yu Tseng, Ayush Saraf, Changil Kim, Yung-Yu Chuang, Johannes Kopf, and Jia-Bin Huang. Robust dynamic radiance fields. In *CVPR*, 2023. 2
- [26] Li Ma, Vasu Agrawal, Haithem Turki, Changil Kim, Chen Gao, Pedro Sander, Michael Zollhöfer, and Christian Richardt. Specnerf: Gaussian directional encoding for specular reflections. *arXiv preprint arXiv:2312.13102*, 2023. 2
- [27] Marko Mihajlovic, Sergey Prokudin, Siyu Tang, Robert Maier, Federica Bogo, Tony Tung, and Edmond Boyer. Splatfields: Neural gaussian splats for sparse 3d and 4d reconstruction. *arXiv preprint arXiv:2409.11211*, 2024. 2
- [28] Jacob Munkberg, Jon Hasselgren, Tianshang Shen, Jun Gao, Wenzheng Chen, Alex Evans, Thomas Müller, and Sanja Fidler. Extracting Triangular 3D Models, Materials, and Lighting From Images. In *Proceedings of the IEEE/CVF Conference on Computer Vision and Pattern Recognition (CVPR)*, pages 8280–8290, 2022. 2, 3
- [29] Keunhong Park, Utkarsh Sinha, Jonathan T. Barron, Sofien Bouaziz, Dan B Goldman, Steven M. Seitz, and Ricardo Martin-Brualla. Nerfies: Deformable neural radiance fields, 2021. 2

- [30] Keunhong Park, Utkarsh Sinha, Peter Hedman, Jonathan T. Barron, Sofien Bouaziz, Dan B Goldman, Ricardo Martin-Brualla, and Steven M. Seitz. Hypernerf: A higher-dimensional representation for topologically varying neural radiance fields, 2021. [2](#), [5](#), [6](#), [7](#), [12](#), [13](#), [14](#)
- [31] Sida Peng, Yunzhi Yan, Qing Shuai, Hujun Bao, and Xiaowei Zhou. Representing volumetric videos as dynamic mlp maps, 2023. [2](#)
- [32] Albert Pumarola, Enric Corona, Gerard Pons-Moll, and Francesc Moreno-Noguer. D-nerf: Neural radiance fields for dynamic scenes, 2020. [2](#)
- [33] Yahao Shi, Yanmin Wu, Chenming Wu, Xing Liu, Chen Zhao, Haocheng Feng, Jingtuo Liu, Liangjun Zhang, Jian Zhang, Bin Zhou, et al. Gir: 3d gaussian inverse rendering for relightable scene factorization. *arXiv preprint arXiv:2312.05133*, 2023. [2](#)
- [34] Liangchen Song, Anpei Chen, Zhong Li, Zhang Chen, Lele Chen, Junsong Yuan, Yi Xu, and Andreas Geiger. Nerfplayer: A streamable dynamic scene representation with decomposed neural radiance fields, 2023. [2](#)
- [35] Pratul P. Srinivasan, Boyang Deng, Xiuming Zhang, Matthew Tancik, Ben Mildenhall, and Jonathan T. Barron. Nerv: Neural reflectance and visibility fields for relighting and view synthesis, 2020. [2](#)
- [36] Colton Stearns, Adam Harley, Mikaela Uy, Florian Dubost, Federico Tombari, Gordon Wetzstein, and Leonidas Guibas. Dynamic gaussian marbles for novel view synthesis of casual monocular videos. *arXiv preprint arXiv:2406.18717*, 2024. [2](#)
- [37] Edgar Tretschk, Ayush Tewari, Vladislav Golyanik, Michael Zollhöfer, Christoph Lassner, and Christian Theobalt. Non-rigid neural radiance fields: Reconstruction and novel view synthesis of a dynamic scene from monocular video, 2021. [2](#)
- [38] Dor Verbin, Peter Hedman, Ben Mildenhall, Todd Zickler, Jonathan T Barron, and Pratul P Srinivasan. Ref-nerf: Structured view-dependent appearance for neural radiance fields. In *2022 IEEE/CVF Conference on Computer Vision and Pattern Recognition (CVPR)*, pages 5481–5490. IEEE, 2022. [2](#)
- [39] Dor Verbin, Ben Mildenhall, Peter Hedman, Jonathan T Barron, Todd Zickler, and Pratul P Srinivasan. Eclipse: Disambiguating illumination and materials using unintended shadows. In *Proceedings of the IEEE/CVF Conference on Computer Vision and Pattern Recognition*, pages 77–86, 2024. [2](#)
- [40] Dor Verbin, Pratul P Srinivasan, Peter Hedman, Ben Mildenhall, Benjamin Attal, Richard Szeliski, and Jonathan T Barron. Nerf-casting: Improved view-dependent appearance with consistent reflections. *arXiv preprint arXiv:2405.14871*, 2024. [2](#)
- [41] Bruce Walter, Stephen R Marschner, Hongsong Li, and Kenneth E Torrance. Microfacet models for refraction through rough surfaces. *Rendering techniques*, 2007:18th, 2007. [3](#)
- [42] Qianqian Wang, Vickie Ye, Hang Gao, Jake Austin, Zhengqi Li, and Angjoo Kanazawa. Shape of motion: 4d reconstruction from a single video. *arXiv preprint arXiv:2407.13764*, 2024. [2](#)
- [43] Guanjun Wu, Taoran Yi, Jiemin Fang, Lingxi Xie, Xiaopeng Zhang, Wei Wei, Wenyu Liu, Qi Tian, and Xinggang Wang. 4d gaussian splatting for real-time dynamic scene rendering. *arXiv preprint arXiv:2310.08528*, 2023. [2](#), [6](#), [12](#), [14](#)
- [44] Wenqi Xian, Jia-Bin Huang, Johannes Kopf, and Changil Kim. Space-time neural irradiance fields for free-viewpoint video, 2021. [2](#)
- [45] Zhiwen Yan, Chen Li, and Gim Hee Lee. Nerf-ds: Neural radiance fields for dynamic specular objects. In *Proceedings of the IEEE/CVF Conference on Computer Vision and Pattern Recognition*, pages 8285–8295, 2023. [5](#), [6](#), [11](#), [12](#), [13](#), [14](#)
- [46] Jinyu Yang, Mingqi Gao, Zhe Li, Shang Gao, Fangjing Wang, and Feng Zheng. Track anything: Segment anything meets videos. *arXiv preprint arXiv:2304.11968*, 2023. [11](#), [12](#)
- [47] Ziyi Yang, Xinyu Gao, Wen Zhou, Shaohui Jiao, Yuqing Zhang, and Xiaogang Jin. Deformable 3d gaussians for high-fidelity monocular dynamic scene reconstruction. *arXiv preprint arXiv:2309.13101*, 2023. [2](#), [6](#), [11](#), [12](#), [14](#)
- [48] Ziyi Yang, Xinyu Gao, Yangtian Sun, Yihua Huang, Xiaoyang Lyu, Wen Zhou, Shaohui Jiao, Xiaojuan Qi, and Xiaogang Jin. Spec-gaussian: Anisotropic view-dependent appearance for 3d gaussian splatting, 2024. [2](#)
- [49] Keyang Ye, Qiming Hou, and Kun Zhou. 3d gaussian splatting with deferred reflection. In *ACM SIGGRAPH 2024 Conference Papers*, pages 1–10, 2024. [2](#)
- [50] Wang Yifan, Felice Serena, Shihao Wu, Cengiz Öztireli, and Olga Sorkine-Hornung. Differentiable surface splatting for point-based geometry processing. *ACM Transactions on Graphics (TOG)*, 38(6):1–14, 2019. [2](#)
- [51] Jingyang Zhang, Yao Yao, Shiwei Li, Jingbo Liu, Tian Fang, David McKinnon, Yanghai Tsin, and Long Quan. Neilf++: Inter-reflectable light fields for geometry and material estimation, 2023. [2](#)
- [52] Kai Zhang, Fujun Luan, Qianqian Wang, Kavita Bala, and Noah Snavely. Physg: Inverse rendering with spherical gaussians for physics-based material editing and relighting. In *Proceedings of the IEEE/CVF Conference on Computer Vision and Pattern Recognition*, pages 5453–5462, 2021. [2](#)
- [53] Xiuming Zhang, Pratul P. Srinivasan, Boyang Deng, Paul Debevec, William T. Freeman, and Jonathan T. Barron. Nef-factor: neural factorization of shape and reflectance under an unknown illumination. *ACM Transactions on Graphics*, 40(6):1–18, 2021.
- [54] Xiaoming Zhao, Pratul P Srinivasan, Dor Verbin, Keunhong Park, Ricardo Martin Brualla, and Philipp Henzler. Illuminerf: 3d relighting without inverse rendering. *arXiv preprint arXiv:2406.06527*, 2024. [2](#)
- [55] Zuo-Liang Zhu, Beibei Wang, and Jian Yang. Gs-ror: 3d gaussian splatting for reflective object relighting via sdf priors. *arXiv preprint arXiv:2406.18544*, 2024. [2](#)

## A. Overview

Supplementary material goes here. This supplementary material presents additional results to complement the main manuscript. In Section B, we detail our coarse-to-fine training strategy, along with the network architectures of the deformable Gaussian MLP and deformable reflection MLP. Subsequently, Section C presents additional results, including comprehensive comparisons, more visualizations, training and rendering efficiency, and further ablation studies. Finally, in Section D, we discuss the limitation of our approach and provide visual example of failure case. In addition to this document, we provide an HTML interface to compare our video results with state-of-the-art methods.

## B. Implementation Details

We use PyTorch as our framework and 3DGS [15] as our codebase. Our coarse-to-fine training strategy is divided into three sequential stages: static, dynamic, and specular stages.

**Static stage.** In the static stage, we train the vanilla 3D Gaussian Splatting (3DGS) for 3000 iterations to stabilize the static geometry.

**Dynamic stage.** After the static stage, we move on to the dynamic stage. During this phase, we introduce a deformable Gaussian MLP to model dynamic objects. First, we optimize both the canonical Gaussians and the deformable Gaussian MLP for 3,000 iterations until the scene reaches a relatively stable state. Then, we introduce the normal loss  $\mathcal{L}_{\text{normal}}$ , enabling simultaneous optimization of the scene's normal and depth, and perform an additional 3,000 iterations to further refine the geometry. The dynamic stage comprises a total of 6,000 training iterations.

**Specular stage.** After the dynamic stage concludes, we transition to the specular stage, which involves changing the color representation from complete spherical harmonics to  $\mathbf{c}_{\text{final}}$ . To mitigate potential geometry disruptions due to the initially incomplete  $\mathbf{c}_{\text{final}}$ , we fix the deformable Gaussian MLP and all 3D Gaussian attributes except for zero-order SH, specular tint, and roughness, while temporarily suspending densification. After 6000 iterations, once  $\mathbf{c}_{\text{final}}$  becomes more complete, we resume optimization of all parameters and reinstate the densification process. Concurrently, during the first 2000 iterations of the specular stage, we optimize only the canonical environment map to learn time-invariant lighting. For the canonical environment map, we use  $6 \times 128 \times 128$  learnable parameters. Subsequently, we begin optimizing the deformable reflection MLP to capture time-varying lighting effects until the training is complete. The specular stage comprises a total of 31,000 training iterations.

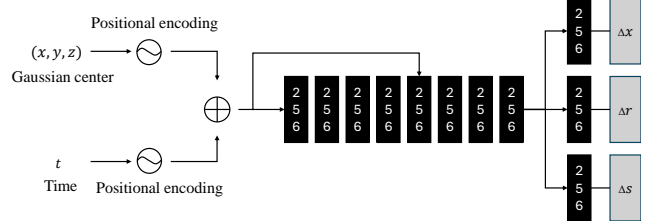


Figure 11. Architecture of the deformable Gaussian MLP

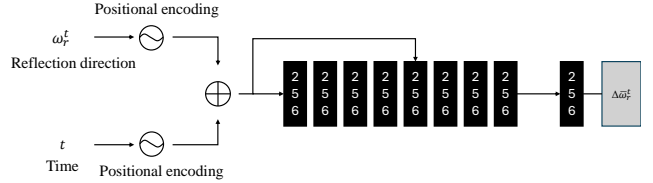


Figure 12. Architecture of the deformable reflection MLP

For the entire experiment, we train for a total of 40,000 iterations and we use Adam optimizer.

### B.1. Network Architecture of the Deformable Gaussian MLP and Deformable reflection MLP

We follow Deformable 3DGS [47] and use deformable Gaussian MLP to predict each coordinate of 3D Gaussians and time to their corresponding deviations in position, rotation, and scaling. As shown in Fig. 11, the MLP initially processes the input through eight fully connected layers that employ ReLU activations, featuring 256-dimensional hidden layers and outputs a 256-dimensional feature vector. This vector is then passed through three additional fully connected layers combined with ReLU activation to separately output the offsets over time for position, rotation, and scaling. Notably, similar to NeRF, the feature vector and the input are concatenated in the fourth layer. For the deformable reflection MLP, we utilize the same network architecture, as shown in Fig. 12.

## C. Additional Results

### C.1. Dynamic specular object of NeRF-DS dataset.

Since each scene in the NeRF-DS dataset [45] contains not only dynamic specular objects but also static background objects, we use Track Anything [46] to obtain masks for the dynamic specular objects. This allows us to evaluate only the dynamic specular objects. As shown in Tab. 7 and Fig. 13, our method outperforms baselines when evaluating the dynamic specular objects in these monocular sequences.

Table 7. **Quantitative comparison on the NeRF-DS [45] dataset with our labeled dynamic specular masks.** We report PSNR, SSIM, and LPIPS (VGG) of previous methods on dynamic specular objects using the dynamic specular objects mask generated by Track Anything [46]. The **best**, the **second best**, and **third best** results are denoted by red, orange, yellow.

Method	As			Basin			Bell			Cup		
	PSNR↑	SSIM↑	LPIPS↓									
Deformable 3DGS [47]	24.14	0.7432	0.2957	17.45	0.5530	0.3138	19.42	0.5516	0.2940	20.10	0.5446	0.3312
4DGS [43]	22.70	0.6993	0.3517	16.61	0.4797	0.4084	14.64	0.2596	0.4467	18.90	0.4132	0.4032
GaussianShader [11]	19.27	0.5652	0.5232	15.71	0.4163	0.5941	12.10	0.1676	0.6764	14.90	0.3634	0.6146
GS-IR [22]	19.32	0.5857	0.4782	15.21	0.4009	0.5644	12.09	0.1757	0.6722	14.80	0.3445	0.6046
NeRF-DS [45]	23.67	0.7478	0.3635	17.98	0.5537	0.4211	14.73	0.2439	0.5931	19.95	0.5079	0.3494
HyperNeRF [30]	17.37	0.6934	0.3834	18.75	0.5671	0.4125	13.93	0.2292	0.6051	15.07	0.4860	0.4183
Ours	24.51	0.7534	0.2896	17.71	0.5675	0.3048	19.60	0.5680	0.2862	20.28	0.5473	0.3176
Method	Plate			Press			Sieve			Mean		
	PSNR↑	SSIM↑	LPIPS↓									
Deformable 3DGS [47]	16.12	0.5192	0.3544	19.64	0.6384	0.3268	20.74	0.5283	0.3109	19.66	0.5826	0.3181
4DGS [43]	13.93	0.4095	0.4229	20.17	0.5434	0.4339	19.70	0.4498	0.3879	18.09	0.4649	0.4078
GaussianShader [11]	9.87	0.2992	0.6812	16.84	0.4408	0.6093	16.19	0.3241	0.5862	14.98	0.3681	0.6121
GS-IR [22]	11.09	0.3254	0.6270	16.43	0.4083	0.5776	16.42	0.3339	0.5749	15.05	0.3678	0.5856
NeRF-DS [45]	14.80	0.4518	0.3987	19.77	0.5835	0.5035	20.28	0.5173	0.4067	18.74	0.5151	0.4337
HyperNeRF [30]	16.03	0.4629	0.3775	14.10	0.5365	0.5023	18.39	0.5296	0.3949	16.23	0.5007	0.4420
Ours	16.53	0.5369	0.3041	21.70	0.6630	0.3252	20.36	0.5089	0.3190	20.10	0.5921	0.3066

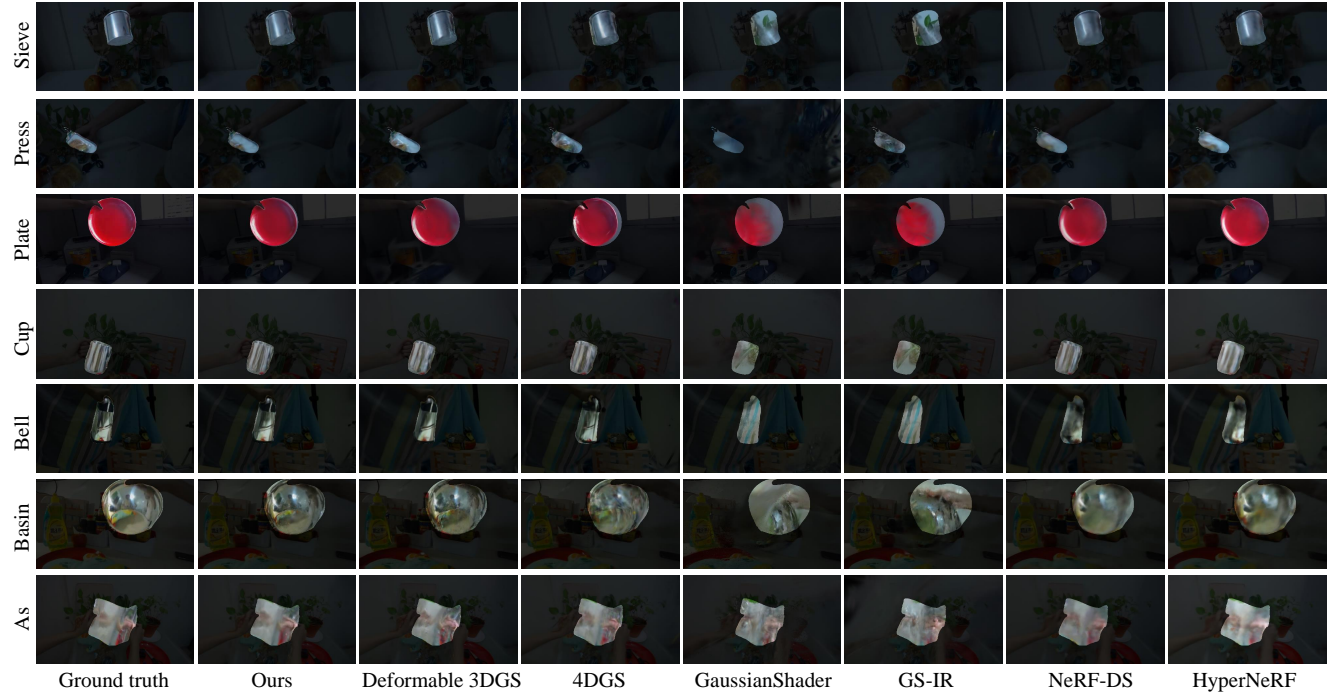


Figure 13. Qualitative comparison on NeRF-DS [45] dataset with labeled dynamic specular masks.

## C.2. Per-Scene results on the NeRF-DS and HyperNeRF Dataset

In Fig. 14, we present qualitative results for each scene in the NeRF-DS dataset [45]. The visualizations demonstrate that

our method achieves superior rendering quality compared to other approaches. We also provide rendered test images and their corresponding normal maps and depth maps for each scene in the NeRF-DS dataset in Fig. 15. Additionally, in

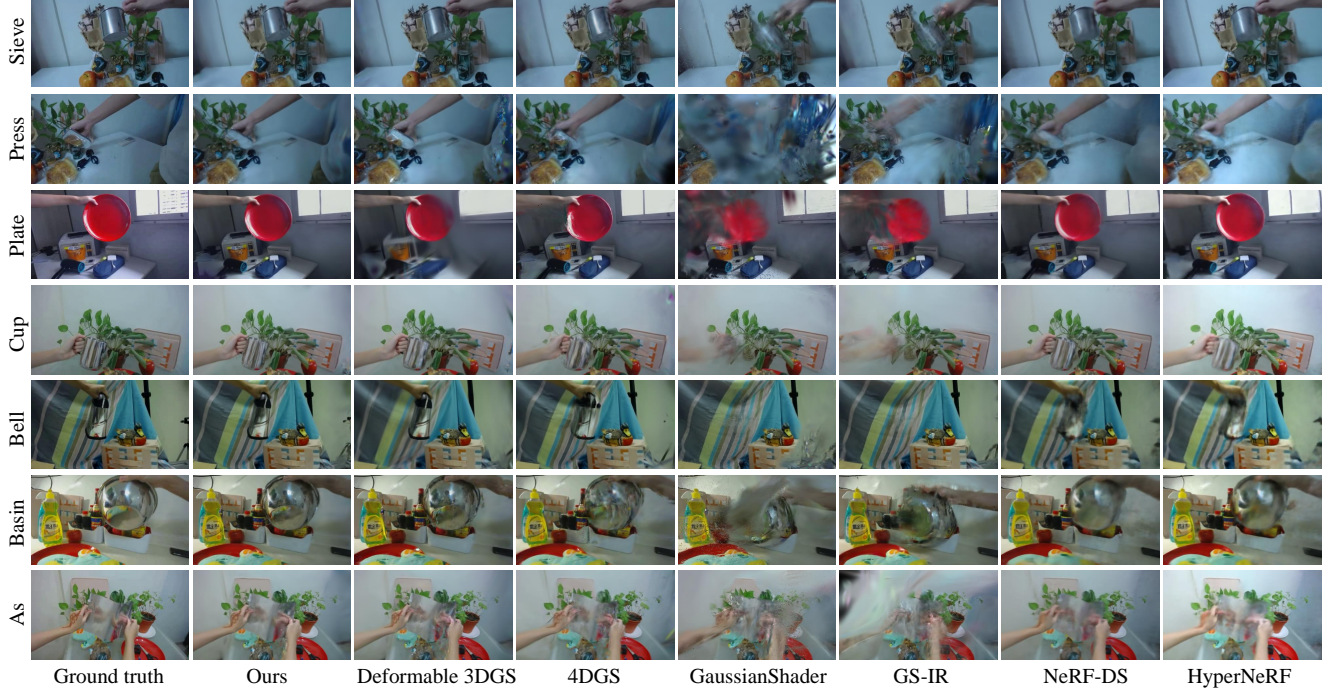


Figure 14. Qualitative comparison on the NeRF-DS [45] dataset.

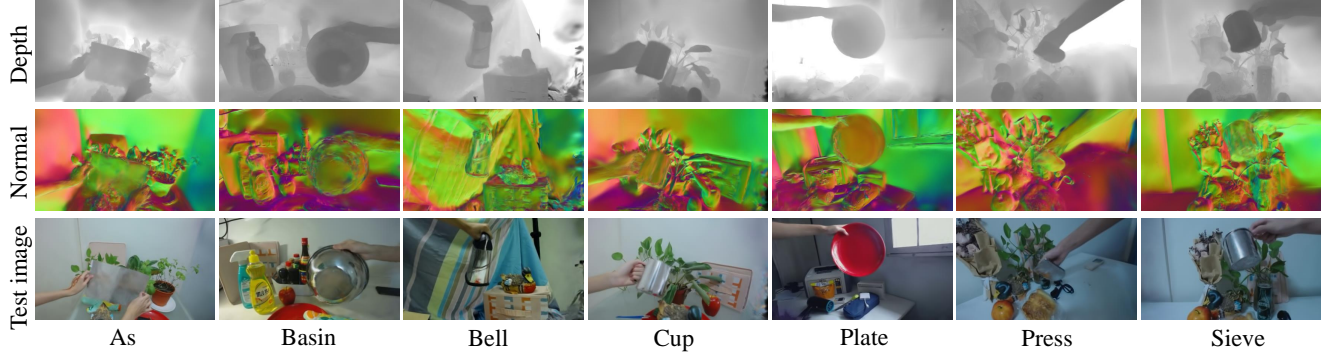


Figure 15. Visualized our rendered test images, normal maps, and depth maps.

Tab. 8, we provide quantitative comparisons for each scene in the HyperNeRF dataset [30], showing that our method remains competitive with existing approaches even in scenes without specular objects.

### C.3. Deformation magnitudes and color decomposition

Unlike NeRF-DS [45], our approach does not require mask supervision to clearly distinguish between static and dynamic objects, as illustrated in Fig. 16. Additionally, Fig. 17 illustrates our method’s decomposition results. As shown, our approach consistently achieves a realistic separation of specular and diffuse components across different scenes in the NeRF-DS dataset [45].

### C.4. Training and rendering efficiency

In Tab. 9, we present the training time, FPS, and number of Gaussians from our experiments on each scene in the NeRF-DS dataset [45]. The results show that for scenes with fewer than 178k Gaussians, our method achieves real-time rendering greater than or equal to 30 FPS. Our experiments are conducted on an NVIDIA RTX 4090 GPU.

### C.5. Ablation study on different $\gamma^k$

In Tab. 10 and Fig. 18, we examine how varying the exponent  $k$  in  $\gamma^k$  impacts the results and we conduct experiments on the NeRF-DS dataset [45]. We observe optimal results when  $k=5$ . When  $k$  is too small,  $\mathcal{L}_{\text{reg}}$  becomes larger, causing normal residuals to become smaller, leading to less flat 3D

Table 8. **Quantitative comparison on the HyperNeRF [30] dataset.** We report the average PSNR, SSIM, and LPIPS (VGG) of several previous models. The **best**, the **second best**, and **third best** results are denoted by red, orange, yellow.

Method	Broom			3D printer			Chicken			Peel Banana			Mean		
	PSNR↑	SSIM↑	LPIPS↓	PSNR↑	SSIM↑	LPIPS↓	PSNR↑	SSIM↑	LPIPS↓	PSNR↑	SSIM↑	LPIPS↓	PSNR↑	SSIM↑	LPIPS↓
Deformable 3DGS [47]	20.87	0.3202	0.5985	20.35	0.6673	0.3091	22.63	0.6346	0.2616	27.27	0.8584	0.1828	22.78	0.6201	0.3380
4DGS [43]	21.21	0.3555	0.5669	21.90	0.6993	0.3198	28.69	0.8143	0.2772	27.77	0.8431	0.2049	24.89	0.6781	0.3422
GaussianShader [11]	17.21	0.2263	0.5812	17.31	0.5926	0.5054	19.70	0.6520	0.5004	19.99	0.7097	0.3308	18.55	0.5452	0.4795
GS-IR [22]	20.46	0.3420	0.5229	18.24	0.5745	0.5204	20.64	0.6592	0.4536	20.15	0.7159	0.3021	19.87	0.5729	0.4498
NeRF-DS [45]	22.37	0.4371	0.5694	22.16	0.6973	0.3134	27.32	0.7949	0.3139	22.75	0.6328	0.3919	23.65	0.6405	0.3972
HyperNeRF [30]	20.72	0.4276	0.5773	21.94	0.7003	0.3090	27.40	0.8013	0.3052	22.36	0.6257	0.3956	23.11	0.6387	0.3968
Ours	19.82	0.2779	0.4892	19.83	0.6538	0.3212	21.49	0.6122	0.2727	27.58	0.8624	0.1742	22.18	0.6016	0.3143

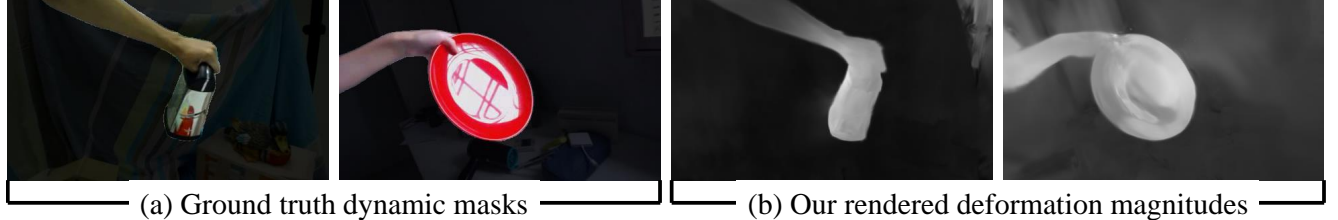


Figure 16. **Visualized our deformation magnitudes.** (a) The left side shows the ground truth of the dynamic object, while (b) on the right side, we render the magnitude of the output of the position residual by our deformable Gaussian MLP. The brighter areas indicate greater movement of the 3D Gaussians. The figure shows that even without mask supervision, our method can still effectively distinguish which objects are dynamic.

Table 9. **Training and rendering efficiency on NeRF-DS [45] dataset**

Scene	Training time (hr)	FPS	Number of Gaussians (k)
as	1.2	31	170
basin	1.3	25	218
bell	1.9	18	335
cup	1.7	30	177
plate	1.1	27	187
press	1.0	31	172
sieve	1.1	29	178

Table 10. **Ablation study on different  $\gamma^k$**

	PSNR ↑	SSIM ↑	LPIPS ↓
$\gamma^k, k = 0$	24.09	0.8515	0.1818
$\gamma^k, k = 1$	24.14	0.8523	0.1786
$\gamma^k, k = 5$	<b>24.17</b>	<b>0.8529</b>	<b>0.1778</b>
$\gamma^k, k = 50$	24.11	0.8521	0.1793

Gaussians whose shortest axis significantly deviates from the surface normal. The insufficient normal residuals correction causes these 3D Gaussians’ shortest axes to deviate greatly from their original direction in an attempt to align with the surface normal, ultimately reducing rendering quality. Conversely, when  $k$  is too large,  $\mathcal{L}_{\text{reg}}$  becomes smaller, causing normal residuals to become larger, allowing some

Table 11. **Ablation study on different  $\lambda_{\text{normal}}$**

	PSNR ↑	SSIM ↑	LPIPS ↓
$\lambda_{\text{normal}} = 1$	8.35	0.1031	0.5954
$\lambda_{\text{normal}} = 0.1$	15.14	0.4379	0.4529
$\lambda_{\text{normal}} = 0.01$	<b>24.17</b>	<b>0.8529</b>	<b>0.1778</b>
$\lambda_{\text{normal}} = 0.001$	24.13	0.8522	0.1796
$\lambda_{\text{normal}} = 0.0001$	24.10	0.8520	0.1803

3D Gaussians’ normal residuals to dominate normal optimization, resulting in insufficient optimization of the 3D Gaussians’ shortest axis towards the correct normal, which in turn reduces the rendering quality.

### C.6. Ablation study on different $\lambda_{\text{normal}}$

In Tab. 11 and Fig. 19, we analyze the impact of different  $\lambda_{\text{normal}}$  values on our results, and we find that the best result is achieved when  $\lambda_{\text{normal}} = 0.01$ . From Tab. 11, we can observe that when  $\lambda_{\text{normal}} \geq 0.1$ , the results deteriorate significantly. This occurs because when  $\lambda_{\text{normal}} \geq 0.1$ , the normal loss becomes too large, leading to unstable training and causing some scenes to collapse during the training process. We conduct experiments on the NeRF-DS dataset [45].

### D. Limitation

In some dramatic scenes, relying solely on the deformable Gaussian MLP and coarse-to-fine training strategy is insuffi-

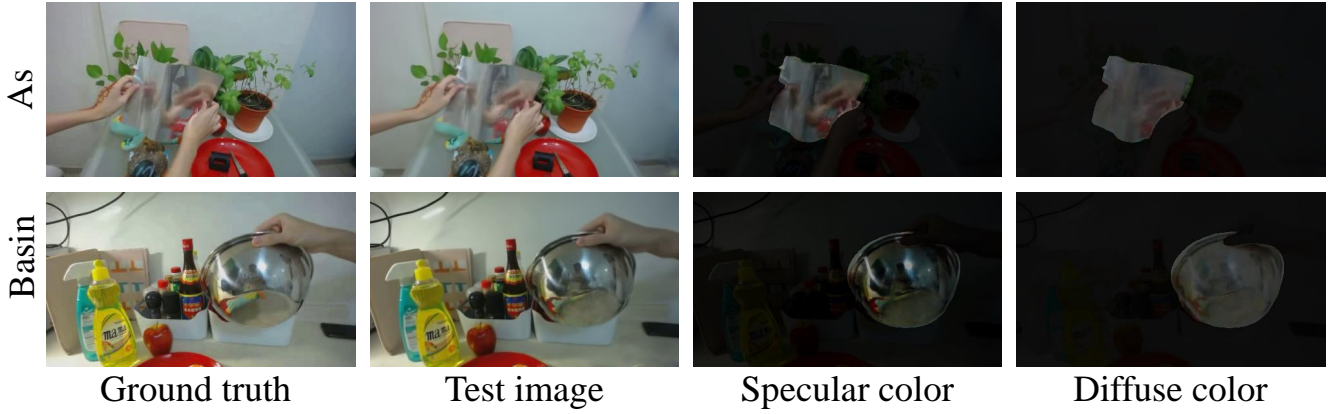


Figure 17. **Visualized our specular and diffuse color.** Specular regions are emphasized while non-specular areas are dimmed to highlight the results of specular region color decomposition.



Figure 18. **Qualitative comparison on different  $\gamma^k$ .**

cient, such as when an arm or body enters or exits the scene, leading to many floaters occurring. We provide visual results in Fig. 20.

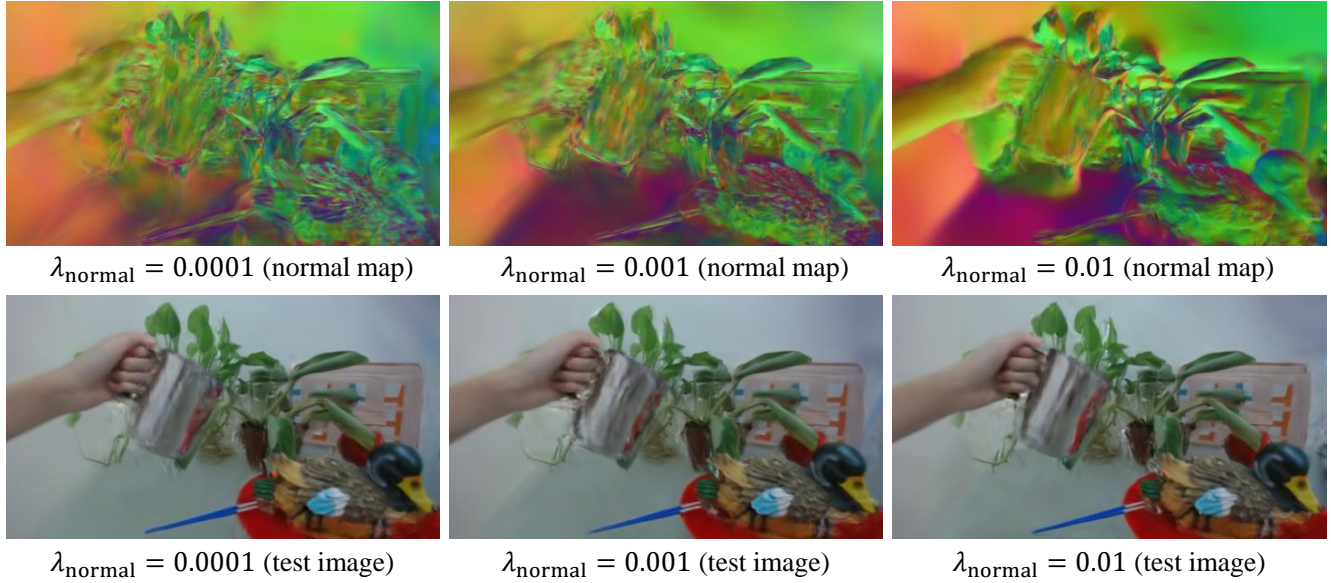


Figure 19. **Qualitative comparison on different  $\lambda_{\text{normal}}$ .**



Dramatic scenes

Figure 20. **Failure cases of modeling dramatic scene changes.** There are dramatic scenes where an arm or body enters or exits the scene, leading to many floaters occurring.